ChemPubSoc Europe

DOI: 10.1002/chem.201704251

CHEMISTRY
A European Journal
Communication

Biosensors |Hot Paper|

A Signal on Photoelectrochemical Biosensor Based on Bismuth @N,O-Codoped Carbon Core-Shell Nanohybrids for Ultrasensitive Detection of Telomerase in HeLa Cells

Shanshan Liu, Shulin Zhao, Wenwen Tu, Xiaoying Wang, Xiao Wang, Jianchun Bao, Yu Wang, Min Han,* and Zhihui Dai*[a]

Abstract: Core-shell nanohybrids (NHs) with good semiconducting properties are vital to promote optoelectronic, photocatalytic, biosensing and bioelectronics technologies. Although great process has been achieved, synthesis of NHs composed of semiconductor core and heteroatom-doped nanocarbon shell remains a challenge, and their applications in photoelectronchemical (PEC) biosensors have not been explored. Herein, the synthesis and properties of a Bi nanocrystal and N,O-codoped carbon (NOC) core–shell NHs (Bi@NOC) is described, which exhibits the typical semiconducting feature with the bandgap of 1.14 eV. Also, such NHs show good biocompatibility and their surfaces bear the carboxylic groups that facilitate further assembly of an amino-modified primer DNA. By taking advantage of the excellent PEC activity of Bi@NOC NHs and the signal amplification effect of thioflavine-T, a novel "signal on" PEC aptasensor for the detection of telomerase activity is constructed. The fabricated aptasensor can detect telomerase activity from 5.0×10^2 to 1.0×10^6 HeLa cells with a low detection limit of 60 cells. Also, the aptasensor shows a wide linear response ranges, high sensitivity and good reproducibility. This work not only enriches current core–shell NHs family but also offers a novel PEC biosensing platform for detecting telomerase activity that is helpful for early clinical diagnosis of cancer.

Human telomerase, a ribonucleoprotein reverse transcriptase containing a protein reverse transcriptase and a RNA component, can catalyze the extension reaction in the 3′ end of chromosomal DNA with the telomeric repeats $(TTAGGG)_n$, and affect cells senescence and apoptosis.[1] Its over-expression is widely observed in most cancer cells, indicating that there is a closed relationship between telomerase activity and cancer.[2] Thus, many efforts have been devoted to detect telomerase activity with the aim for early diagnosis and therapy of cancer. By far, several strategies have been proposed for detecting telomerase activity, including polymerase chain reaction based telomeric repeat amplification protocol, DNA enzyme-based chemiluminescence, fluorescence, electrochemiluminescence, and other electrochemical technologies.[3] Nonetheless, these methods suffer from drawbacks, such as low sensitivity, high overpotential, and tedious fluorescent tagging or complicated operations. To overcome those limitations, it is necessary to develop new and alternative techniques for examining telomerase activity. As a newly developed technique, photoelectrochemical (PEC) biosensors have attracted considerable interest due to their remarkable merits including facile and convenient operation, low background signal, high sensitivity, and good reproducibility.[4] Unfortunately, PEC biosensors have not been developed for the detection of telomerase activity, however they have been used to examine other biomolecules and biomarkers. So, it is highly imperative but challenging to develop PEC biosensors for the analysis of telomerase activity, which is important for the clinical early diagnosis and therapy of cancer.

To fabricate an ultrasensitive PEC biosensor, the key lies on finding highly efficient and robust semiconductor nanostructures with wide optical response ranges as the photoactive materials. Traditionally, Cd-based quantum dots and wide bandgap metal oxide semiconductor (e.g. TiO_2 and ZnO) nanostructures are adopted as the photoactive materials to construct the desired PEC biosensors for detecting specific biomolecules or biomarkers.[5] As for Cd-based quantum dots, they have good optical response, but they are harmful for biomolecules and are easily photo-bleached. Wide bandgap metal oxide semiconductors, are photo-stable and show good PEC activity, but they only respond to ultraviolet light. To improve the biocompatibility, photo-stability, and photo-response range of the PEC biosensors, it is urgent to explore and develop newly photoactive materials. Recently, core–shell nanohybrids (NHs) with the typical semiconducting features, such as CdS@ZnS, Sb@C, and CdS@CdSe nanoparticles, TiO_2@FeMnP nanorods, and CdS@Cu_2S nanowires, have aroused much attention due to the passivation of surface vacancies of desired semiconductors and the efficient bandgap modulation, and their applications in optoelectronics and photocatalytic fields have been widely explored.[6] However, their application in PEC

[a] Dr. S. Liu, Dr. S. Zhao, Prof. Dr. W. Tu, X. Wang, X. Wang, Prof. Dr. J. Bao, Y. Wang, Prof. Dr. M. Han, Prof. Dr. Z. Dai
Jiangsu Collaborative Innovation Center of Biomedical Functional Materials and Jiangsu Key Laboratory of Biofunctional Materials
School of Chemistry and Materials Science
Nanjing Normal University, Nanjing 210023 (P. R. China)
E-mail: 07203@njnu.edu.cn
daizhihuii@njnu.edu.cn

Supporting information for this article can be found under: https://doi.org/10.1002/chem.201704251: experimental section, additional characterization for Bi@NOC NHs, the molecular orbital of Th-T, and the optimization of the detection conditions.

biosensors are relatively rare. To the best of our knowledge, there is nearly no report on using core–shell NHs as the photoactive material to fabricate PEC biosensor for detection of telomerase activity until now. So, synthesizing novel semiconducting core–shell NHs and exploring their applications in PEC telomerase biosensors becomes an interesting topic.

Herein, we report the synthesis of novel core–shell NHs composed of Bi nanocrystal core and N, O-codoped nanocarbon (NOC) shell (Bi@NOC), and their application as a PEC telomerase biosensor. The typical synthesis is based on low-temperature liquid-phase carbonization of folic acid in the presence of $Bi(Ac)_3$ and oleylamine. The Bi salt precursor is firstly reduced by oleylamine to form the Bi nanocrystals cores, which catalyzes or promotes the conversion or carbonization of folic acid molecules to generate NOC that is covered on the surface of Bi nanocrystals cores. In the obtained NHs, the Bi nanocrystal core is a semiconductor with a small bandgap, which can be easily excited by the visible light to generate weak photocurrent.[7] As for the NOC "envelope", it possesses an excellent biocompatibility because it derives from folic acid. Additionally, the NOC shell layers have high charge carrier mobility and super electron accept ability,[8] facilitating to enhance the interfacial electron transfer rate and inhibit the electron-hole recombination in Bi nanocrystals core that is beneficial to improve photoelectric conversion efficiency and photocurrent intensity. Also, the fermi level alignment between Bi nanocrystals core and NOC shell favors the separation of photo-generated charge carriers, helpful for generation of photocurrent.[8] Thus, such Bi@NOC NHs exhibit an excellent PEC activity under the irradiation of visible light, offering a promising platform for integration of other signal magnification reagents to construct desired PEC biosensing system. As a fluorescent dye, thioflavin T (Th-T) can recognize telomeres extended sequence and bind with it to form the G-quadruplex.[9] The introduction of Th-T can significantly enhance the photocurrent signal of the PEC system by using the Bi@NOC NHs as the photoactive material and ascorbic acid as the electrons donor. Based on this experimental phenomenon, a novel "signal on" PEC aptasensor for the detection of telomerase activity is fabricated by taking advantage of the excellent PEC activity of the Bi@NOC NHs and the signal enhancement effect of Th-T/G-quadruplex (Scheme 1). The fabricated PEC aptasensor can detect the telomerase activity from 5.0×10^2 to 1.0×10^6 HeLa cells with a low detection limit of 60 cells. Moreover, the aptasensor also possesses a wide linear response range, high sensitivity and good reproducibility, showing a great potential to be applied in early clinical diagnosis of cancer.

The makeup, phase structure and crystallinity of the as-synthesized Bi@NOC NHs were characterized by the X-ray diffraction (XRD), Raman and the X-ray photoelectron spectroscopies (XPS). Figure 1 A shows the XRD pattern of the Bi@NOC NHs. The twenty-two diffraction peaks are observed at the 2θ of 22.5°, 23.8°, 27.3°, 37.9°, 39.8°, 44.6°, 45.9°, 48.8°, 56.2°, 59.3°, 61.08°, 62.1°, 64.5°, 67.4°, 70.7°, 71.9°, 73.7°, 75.3° and 81.09° can be indexed to the (003), (101), (012), (104), (110), (015), (113), (202), (024), (107), (205), (116), (122), (018), (214), (009), (027), (125) and (208) planes of Bi with cubic phase structure

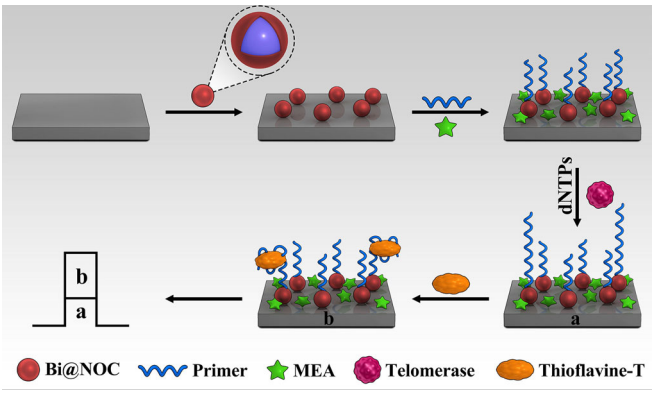

Scheme 1. Illustration of the PEC biosensor for telomerase detection based on the superb PEC activity of Bi@NOC NHs and the signal amplification effect of Th-T.

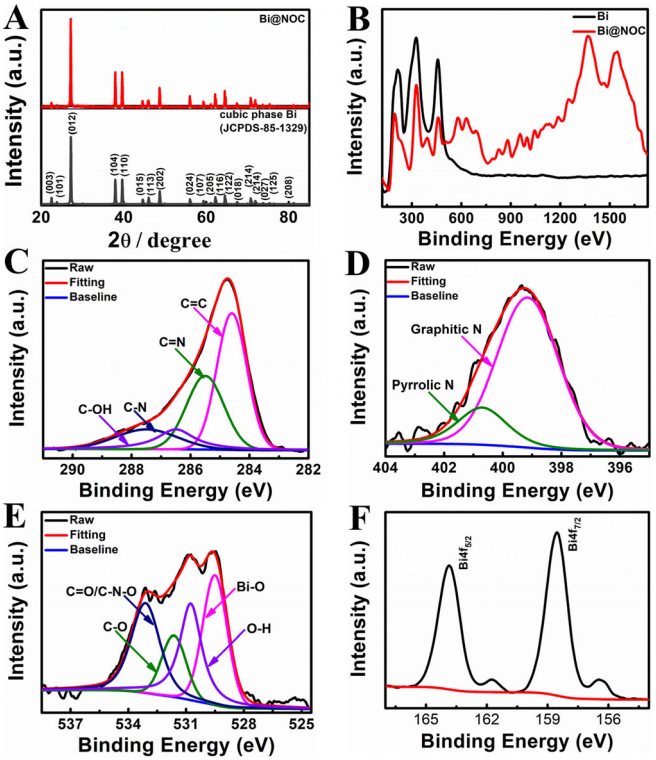

Figure 1. A–B) XRD pattern (A) and Raman spectrum (B) of the as-synthesized Bi@NOC NHs. C–F) The related core-level fine XPS spectra for C 1s (C), N1s (D), O1s (E) and Bi 4f (F), respectively.

(JCPDS-85–1329),[10] respectively. The high diffraction peak intensity of Bi depresses the diffraction peak of NOC component. Additionally, due to the low-temperature liquid-phase carbonization, the graphitic degree of the NOC component may be low. Moreover, the NOC shell layer is very thin, which may weaken the diffraction signal. Thus, the diffraction peaks from the NOC component can't be seen clearly in Figure 1 A. To confirm the existence of the NOC component, Raman spectrum tests were performed (Figure 1 B). Compared with that of pure Bi powder, the Bi@NOC NHs also show four featured peaks in the low wavenumber region (178, 205, 310 and 460 cm^{-1}),

proving the presence of Bi nanocrystals component in the NHs. At the high wavenumber region, the Bi@NOC NHs exhibit other two characteristic peaks at 1356 cm^{-1} and 1572 cm^{-1}, which are ascribed to the disorder-induced D-band and the tangential stretch G-band of carbon-based nanostructures, indicating the presence of the NOC component.[11] To further identify the component and chemical states of various elements, the XPS tests are further executed. The related survey XPS spectrum (Supporting Information, Figure S1) shows the presence of C, N, O, and Bi elements in the obtained NHs. As shown in Figure 1C, the C 1s fine spectrum is highly asymmetric. After fitting, it can be deconvoluted into four peaks with the binding energies (BEs) centred at 284.6, 285.5, 286.5 and 287.5 eV, which can be assigned to the formation of C=C, C=N, C bound to O in phenol and ether (i.e., C–OH), and C–N bonds, respectively.[12] This result indicates that the N and O may be co-doped into the C lattice to form the NOC component. Further evidences come from the N 1s and O 1s fine spectra. As illustrated in Figure 1D, the N 1s fine spectrum can be deconvoluted into two featured peaks with the BEs at 399.2 and 400.7 eV, corresponding to the presence of pyrrolic N, and graphitic N species, respectively. Similarly, the O1s fine spectrum (Figure 1E) can be deconvoluted into four characteristic peaks with the BEs at 529.5, 530.8, 531.6, and 533.1 eV, assigning to the formation of Bi–O, O–H, C–O, and C=O/C-N-O bonds, respectively.[13] As for the Bi 4f fine spectrum (Figure 1F), the two small peaks with the BEs at 156.5 and 161.8 eV are the characteristic $4f_{7/2}$ and $4f_{5/2}$ peaks for metallic Bi. As for other two strong peaks at 158.5 and 163.9 eV. They are usually assigned to the $4f_{7/2}$ and $4f_{5/2}$ peaks for Bi^{3+} ions or formation of amorphous Bi oxides.[14] Here, the observed Bi^{3+} ions may result from the outmost layers of Bi cores losing or donating electrons to the NOC shell, which can bind or coordinate with O in the NOC shell to form the well-coupled Bi@NOC NHs. That is to say, in the Bi@NOC NHs, the electrons readily transfer from the Bi cores to NOC shell layer, beneficial to PEC application.

In addition, to further identify the surface structure or exposed functional groups on Bi@NOC NHs, the FT-IR spectrum test is carried out yet, shown in Figure S2 in the Supporting Information. The five characteristic absorption bands that are assigned to C–O, C=O, O–H, C–N, and C–H stretching vibrations are observed at 1043, 1622, 3428, 1380 and 2924 cm^{-1}, respectively, implying that there are carboxylic groups present in the NOC shell layer. This offers the other evidence for the C 1s and O1s fine XPS spectra analysis. The presence of carboxylic groups can improve the hydrophilic of the Bi@NOC NHs, facilitating to further assemble amino-modified primer DNA for construction of the desired PEC aptasensor.

The morphology and microstructure of the Bi@NOC core–shell NHs were further examined by the transmission electron microscopy (TEM) and high-resolution TEM (HRTEM). Figure 2A shows the low magnification TEM image, from which many quasi-spherical nanoparticles with an average size of 60 nm can be observed (Figure S3). From the high-magnification TEM image shown in Figure 2B, the clear core–shell nanostructure composed of the dark core with the larger size (≈100 nm) and

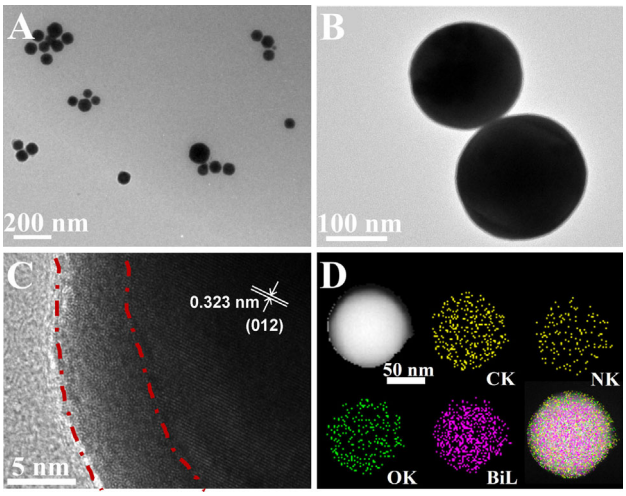

Figure 2. A–B) Low- (A) and High- (B) magnification TEM images of the obtained Bi@NOC NHs. C) HRTEM image for an individual Bi@NOC nanostructure. D) Related HAADF-STEM image and elemental mapping analysis for an individual Bi@NOC nanostructure.

thin (≈5 nm) light-colored shell layer can be seen. According to their difference, the dark core is the Bi nanocrystal. While the light-colored shell layer is the NOC component. The corresponding HRTEM image for an individual Bi@NOC nanostructure is shown in Figure 2C. For the core region, the clear lattice fringes with the spacing of 3.23 Å is observed, corresponding to the interplanar separation between (012) plane of the cubic phase Bi (JCPDS-85–1239). As for the shell layer region (the red dotted lines indicated), no obvious lattice fringes can be observed, indicating that the graphitic degree of the NOC is low. The related high-angle annular dark field-scanning transmission microscopy (HAADFSTEM) image and elemental mapping analysis for an individual Bi@NOC nanostructure disclose that the C, O, N elements are distributed at the edges regions whereas the Bi element is mainly distributed at the middle or core region, further confirming the formation of core–shell structures in the obtained NHs.

To examine the optical bandgap of the Bi@NOC NHs, the reflection spectrum of the solid sample is measured. By using the Kubelka–Munk function,[15] the diffused absorption spectrum *F(R)* of the Bi@NOC NHs is obtained, shown in Figure 3A. The clear and sharp absorption edge can be observed at the wavelength of 510 nm. Supposing that the absorption is a

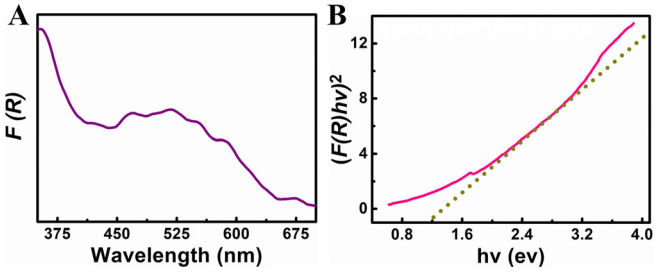

Figure 3. A) The diffused absorption spectrum *F(R)* of the Bi@NOC NHs. (b) The plot of $(F(R)h\nu)^2$ versus $h\nu$.

direct allowed transition, the bandgap energy (E_g) of the Bi@NOC NHs can be obtained from the energy intercept of a plot of $(F(R)h\nu)^2$ versus $h\nu$. A corresponding plot of $(F(R)h\nu)^2$ versus $h\nu$ is shown in Figure 3B, from which the E_g of the Bi@NOC NHs is calculated to be about 1.14 eV. In relative to the wide bandgap semiconductor materials such as TiO_2 and ZnO,[16] the narrow bandgap observed in Bi@NOC NHs is highly desirable because it can be excited by the visible light, which can improve the PEC stability of the sensing system and avoid the damage or de-activation of the biomolecules.

To investigate the PEC performance of the Bi@NOC NHs, the photocurrent of pure carbon dots and pure Bi nanocrystals are firstly measured in 0.1 M Tris-HCl buffer (pH 7.4) that containing 5.0 mM of ascorbic acid (AA). As shown in Figure 4A, the PEC

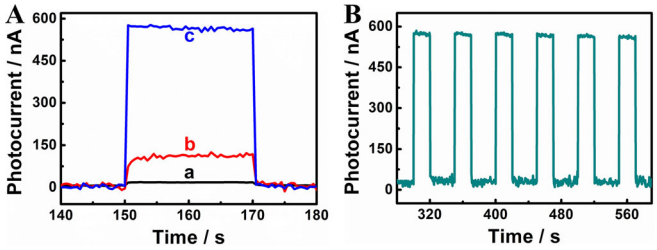

Figure 4. (A) PEC responses of ITO/carbon dots (a), ITO/Bi nanocrystals (b), ITO/ Bi@NOC NHs (c). (B) PEC responses of the Bi@NOC NHs modified ITO electrode at an applied potential of −0.1 V under the irradiation of the light with the wavelength of 405 nm.

intensity of the carbon dots is about 20 nA under the irradiation of the light with the wavelength of 405 nm at an applied potential of −0.1 V (plot a), consistent with that of previous report.[17] When pure Bi nanocrystals are deposited on indium tin oxide (ITO) electrode, the generated cathodic photocurrent is 110 nA (plot b). As a semiconductor with a small bandgap (38 meV),[6a] the photo-generated electron-hole pairs can be formed in pure Bi nanocrystals by excitation with a small energy, and readily recombined, which lead to reduce the photoelectric conversion efficiency, limiting their applications in solar cells and PEC biosensors. When the Bi nanocrystals are coated with a layer of NOC shell, the enhanced photocurrent of 560 nA can be observed on Bi@NOC NHs modified ITO electrode (plot c), which is about 28- and 5-fold higher than those of pure carbon dots and pure Bi nanocrystals modified ITO, respectively. The significant enhancement of photocurrent observed on Bi@NOC NHs modified ITO electrode may be attributed to the dramatically improved photoelectric conversion efficiency. Due to its narrow bandgap, the photo-generated charge carriers excited from Bi nanocrystals are liable to radiative recombination. Once they are covered with NOC shell layer as the efficient acceptors, the photo-generated electrons efficiently transfer from Bi core to NOC shell. Thus, the electron-hole recombination is greatly reduced or restrained, beneficial to improve photoelectric conversion efficiency and enhance photocurrent response. Additionally, protons in the Tris-HCl buffer can capture the electrons from the surface of the NOC shell, and AA served as the sacrificial reagent can scavenge some of the photo-generated holes.[18] It should be mentioned that the enhanced photocurrent is relatively stable after manifold cycles (Figure 4B).

Electrochemical impedance spectroscopy (EIS) was used to characterize the stepwise assembly processes of the PEC aptasensor (Figure 5A). Compared with that of bare ITO electrode

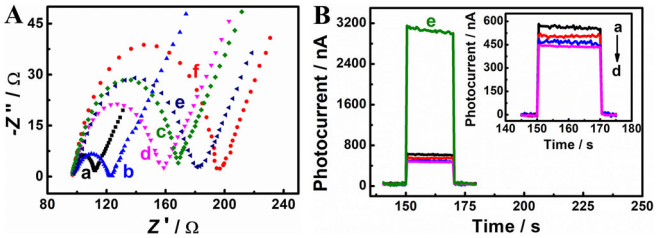

Figure 5. (A) Nyquist diagrams of bare ITO (a), ITO/Bi@NOC NHs (b), ITO/Bi@NOC NHs/DNA (c), ITO/Bi@NOC NHs/DNA/MEA (d), ITO/Bi @NOC NHs/DNA/MEA/elongated DNA (e), ITO/Bi@NOC NHs/DNA/MEA/elongated DNA/Th-T (10^4 cell/mL) (f). (B) PEC responses of ITO/Bi@NOC NHs (a), ITO/Bi@NOC NHs/DNA (b), ITO/Bi@NOC NHs/ DNA/MEA (c), ITO/Bi@NOC NHs/DNA/MEA/elongated DNA (d), ITO/Bi@ NOC NHs/DNA/MEA/elongated DNA/Th-T (10^4 cell/mL) (e). The Inset shows the magnified responses from a–d.

(plot a), the electron transfer resistance (R_{et}) of the Bi@NOC NHs modified electrode shows a clear increase (plot b), which can be attributed to the presence of negatively charged carboxylic groups in the NOC shell layer that hinder the negatively charged probe to access the electrode surface. When the primer DNA is introduced to the modified electrode surface by the amidation of Bi@NOC NHs with the amino-modified primer DNA, the R_{et} further increases due to the poor conductivity of single strand DNA and the negatively charged DNA phosphate backbone (plot c). After being blocked with monoethanolamine (MEA), the R_{et} decreases, which results from the electrostatic interaction between the negatively charged probe and the positively charged MEA (plot d). The subsequent chain extension reaction of telomerase primer DNA with the help of telomerase extraction causes the increase of R_{et} value due to the steric hindrance (plot e), suggesting the successful extension of the telomerase primer DNA. As the Thioflavin T (Th-T) is further introduced, the R_{et} continuously increases (plot f), which may be ascribed to the increased steric hindrance that hinders the redox probe to reach the electrode surface. The variation of R_{et} verifies the successful fabrication of the PEC aptasensors.

Each step for the construction of the aptasensor can also be monitored by the photocurrent response (Figure 5B). Compared with that of the Bi@NOC NHs modified ITO electrode (plot a), the photocurrent intensity or signal gradually decreases by subsequent stepwise immobilization of the primer DNA (plot b), MEA blocking (plot c) and chain extension reaction of telomerase primer DNA (plot d). This may be attributed to the increase of electron transfer resistance and the steric barrier, consistent with the EIS analysis (Figure 5A). After the introduction of Th-T through the formation of G-quadruplex with the human telomeric DNA, an enhanced photocurrent of 3020 nA can be observed, which is nearly about 6 times as high as that of the Bi@NOC NHs modified electrode (plot e). The significant

enhancement of photocurrent by introduction of Th-T may originates from the energy level match of NOC shell and Th-T, facilitating to accelerate electron transfer from the conduction band of the NOC shell to the LUMO (the lowest unoccupied molecular orbit) of the Th-T (−5.971 eV; as show in Figure S4). Meanwhile, as a nontoxic electron donor and sacrificial reagent, AA can scavenge some of the photo-generated holes located on Bi@NOC NHs and HOMO (the highest occupied molecular orbit) of the Th-T (−8.028 eV), which is further advantageous to improve the photoelectric conversion efficiency.[19]

Before PEC cytosensing tests, the detection conditions, such as the concentration of Bi@NOC NHs, the applied potential, the excitation wavelength, the concentration of AA and primer DNA, the incubation time and the concentration of Th-T, are firstly optimized. The details are given in Figure S5–6 in the Supporting Information. Under the optimal conditions, the signal on PEC aptasensor is employed for detection of the telomerase activity from the cell samples. Because the extension process of the primer DNA is controlled by the telomerase activity, the amount of Th-T that induces the formation of G-quadruplex should be enhanced along with the increase of cancer cells, which is proportional to the intensity of photocurrent. It means that the higher density of cells leads to a higher level of telomerase activity and more content of Th-T as well as stronger photocurrent. As shown in Figure 6 A, the closed relationship between the intensity of photocurrent and the concentration of HeLa cells is observed. A good linear relationship can be obtained between the ΔI ($\Delta I = I - I_0$; in which I is the photocurrent when the HeLa cells are at different concentrations and I_0 is the background photocurrent when the HeLa cell concentration was zero) and the logarithmic value of the HeLa cell concentration from 5.0×10^2 to 5.0×10^6 cell/mL (Figure 6 B). The regression equation is ΔI (nA) $= -1559.4 + 805.73 \lg c$ (cell/mL), with a correlation coefficient of 0.997. The corresponding detection limit is estimated to be 60 cell/mL at a signal-to-noise ratio of 3. Compared with that of previous reports,[20] the linear response range of our PEC aptasensor becomes wider, and the detection limit is greatly reduced. In addition, the reproducibility is further evaluated by the relative standard deviation obtained from the six independent electrodes that incubated with telomerase cracking fluid at the same cell concentration (5×10^4 cell/mL). The relative standard deviation is calculated to be around 8.6%, suggesting the good reproducibility of the fabricated signal on PEC aptasensor. Furthermore, the photocurrent against normal cells (BEAS-2B, LO-2 cell) is negligible compared with that of tumor cell (HeLa), which suggesting the feasibility for telomerase detection in this system (Figure S8).[21] These results indicate that the constructed PEC aptasensor can be used for ultrasensitive detection of telomerase activity from HeLa cell, showing great potential to be applied in the early clinical diagnosis of cancers.

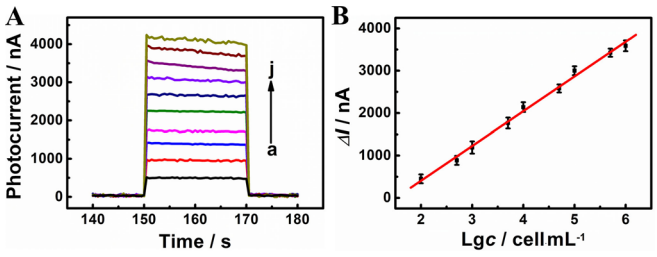

Figure 6. (A) PEC responses of the cytosensor to (a–j) 0, 1×10^2, 5×10^2, 1×10^3, 5×10^3, 1×10^4, 5×10^4, 1×10^5, 5×10^5 and 1×10^6 cells/mL. (B) Linear calibration curve.

In conclusion, novel Bi@NOC NHs have been successfully synthesized for the first time through the low-temperature liquid-phase carbonization of folic acid in the presence of $Bi(Ac)_3$ and oleylamine. Such NHs show the typical semiconducting features with the bandgap of 1.14 eV, which can be easily excited by the visible light. Moreover, their surface bear carboxylic groups, which not only improves the hydrophilicity of the NHs but also facilitates to further assemble amino-modified primer DNA. The presence of NOC shell layer can accelerate the electrons transfer from the Bi cores to NOC shell and solution interface, and significantly decrease the recombination of photo-generated charge carriers, letting the obtained Bi@NOC NHs show excellent PEC activity. Further introduction of thioflavine-T (Th-T) for specifically recognizing telomeres extended sequence (TTAGGG)n to form the G-quadruplex, the PEC response or photocurrent signal can be greatly enhanced, beneficial to PEC sensing application. Thus, by taking advantage of the excellent PEC activity of Bi@NOC NHs and the signal amplification effect of Th-T, a new "signal on" PEC aptasensor is fabricated for examining the telomerase activity. The constructed PEC aptasensor shows a wide linear response range, a low detection limit, high sensitivity and good reproducibility. This work not only enriches current core–shell NHs family but also provides a novel PEC biosensing platform to detect telomerase activity, showing great opportunity for early clinical diagnosis of important diseases.

Acknowledgements

This work was supported by the National Natural Science Foundation of China for the project (21625502, 21475062 and 21671106), the Priority Academic Program Development of Jiangsu Higher Education Institutions.

Conflict of interest

The authors declare no conflict of interest.

Keywords: biosensors · electrochemistry · nanomaterials · photoelectrochemical · telomerase

[1] a) C. B. Harley, *Nat. Rev. Cancer* **2008**, *8*, 167–179; b) M. W. Smith, M. Dean, M. Carrington, C. Winkler, G. A. Huttley, D. A. Lomb, J. J. Goedert, *Science* **1997**, *277*, 955–959; c) F. Rodier, J. J. Campisi, *J. Cell Biol.* **2011**, *192*, 547–556; d) J. S. Wang, C. Q. Zhao, A. D. Zhao, M. Li, J. S. Ren, X. G. Qu, *J. Am. Chem. Soc.* **2015**, *137*, 1213–1219.

[2] a) J. W. Shay, W. E. Wright, *Semin. Cancer Biol.* **2011**, *21*, 349–353; b) C. Y. Xiong, W. B. Liang, Y. N. Zheng, Y. Zhou, Y. Q. Chai, R. Yuan, *Anal. Chem.* **2017**, *89*, 3222–3227.

[3] a) N. W. Kim, F. Wu, *Nucleic Acids Res.* **1997**, *25*, 2595 – 2597; b) Y. Xiao, V. Pavlov, T. Niazov, A. Dishon, M. Kotler, I. Willner, *J. Am. Chem. Soc.* **2004**, *126*, 7430 – 7431; c) Y. Zhuang, C. L. Shang, X. D. Lou, F. Xia, *Anal. Chem.* **2017**, *89*, 2073 – 2079; d) L. Wu, J. S. Wang, L. Y. Feng, J. S. Ren, W. L. Wei, X. G. Qu, *Adv. Mater.* **2012**, *24*, 2447 – 2452; e) P. H. Ling, J. P. Lei, L. Jia, H. X. Ju, *Chem. Commun.* **2016**, *52*, 1266 – 1269; f) Y. Liu, M. Wei, X. Liu, W. Wei, H. Y. Zhao, Y. J. Zhang, S. Q. Liu, *Chem. Commun.* **2016**, *52*, 1796 – 1799.

[4] a) S. G. Ge, F. F. Lan, L. L. Liang, N. Ren, L. Li, H. Y. Liu, M. Yan, J. H. Yu, *ACS Appl. Mater. Interfaces* **2017**, *9*, 6670 – 6678; b) J. Tang, Y. Zhang, B. Kong, Y. Wang, P. Da, J. Li, A. A. Elzatahry, D. Zhao, X. Gong, G. Zheng, *Nano Lett.* **2014**, *14*, 2702 – 2708.

[5] a) Y. Zang, J. P. Lei, L. Zhang, H. X. Ju, *Anal. Chem.* **2014**, *86*, 12362 – 12368; b) Z. Y. Ma, J. B. Pan, C. Y. Lu, W. W. Zhao, J. J. Xu, H. Y. Chen, *Chem. Commun.* **2014**, *50*, 12088 – 12090; c) Z. Y. Yan, Z. H. Wang, Z. Miao, Y. Liu, *Anal. Chem.* **2016**, *88*, 922 – 929; d) X. M. Shi, G. C. Fan, Q. M. Shen, J. J. Zhu, *ACS Appl. Mater. Interfaces* **2016**, *8*, 35091 – 35098.

[6] a) E. Hofman, R. J. Robinson, Z. J. Li, B. Dzikovski, W. W. Zheng, *J. Am. Chem. Soc.* **2017**, *139*, 8878 – 8885; b) J. Liu, L. T. Yu, C. Wu, Y. R. Wen, K. B. Yin, F. K. Chiang, R. Z. Hu, J. W. Liu, L. T. Sun, L. Gu, J. Maier, Y. Yu, M. Zhu, *Nano Lett.* **2017**, *17*, 2034 – 2042; c) N. Razgoniaeva, P. Moroz, M. Yang, D. S. Budkina, H. Eckard, M. Augspurger, D. Khon, A. N. Tarnovsky, M. Zamkov, *J. Am. Chem. Soc.* **2017**, *139*, 7815 – 7822; d) D. E. Schipper, Z. H. Zhao, A. P. Leitner, L. X. Xie, F. Qin, M. K. Alam, S. Chen, D. Z. Wang, Z. F. Ren, Z. M. Wang, J. M. Bao, *ACS Nano* **2017**, *11*, 4051 – 4059; e) J. Y. Tang, Z. Y. Huo, S. Brittman, H. W. Gao, P. D. Yang, *Nat. Nanotechnol.* **2011**, *6*, 568 – 572.

[7] R. Fu, S. Xu, Y. N. Lu, J. J. Zhu, *Cryst. Growth Des.* **2005**, *5*, 1379 – 1385.

[8] Y. Y. Bu, Z. Y. Chen, W. B. Li, B. R. Hou, *ACS Appl. Mater. Interfaces* **2013**, *5*, 12361 – 12368.

[9] J. Mohanty, N. Barooah, V. Dhamodharan, S. Harikrishna, P. I. Pradeepkumar, A. C. Bhasikuttan, *J. Am. Chem. Soc.* **2013**, *135*, 367 – 376.

[10] S. Schulz, S. Heimann, C. Wölper, W. Assenmacher, *Chem. Mater.* **2012**, *24*, 2032 – 2039.

[11] D. C. Wei, Y. Q. Liu, H. L. Zhang, L. P. Huang, B. Wu, J. Y. Chen, G. Yu, *J. Am. Chem. Soc.* **2009**, *131*, 11147 – 11154.

[12] a) Z. Wang, L. Qie, L. Yuan, W. Zhang, X. Hu, Y. Huang, *Carbon* **2013**, *55*, 328 – 334; b) Y. Wang, Y. Shao, D. W. Matson, J. Li, Y. Lin, *ACS Nano* **2010**, *4*, 1790 – 1798.

[13] a) W. Niu, L. Li, X. Liu, N. Wang, J. Liu, W. Zhou, Z. Tang, S. Chen, *J. Am. Chem. Soc.* **2015**, *137*, 5555 – 5562; b) E. McCalla, A. M. Abakumov, M. Saubanère, J. M. Tarascon, *Science* **2015**, *350*, 1516 – 1521; c) L. Liu, W. Liu, X. L. Zhao, D. M. Chen, R. S. Cai, W. Y. Yang, S. Komarneni, D. J. Yang, *ACS Appl. Mater. Interfaces* **2014**, *6*, 16082 – 16090; d) S. J. Zhu, L. L. Lu, Z. W. Zhao, T. Wang, X. Y. Liu, H. J. Zhang, F. Dong, Y. X. Zhang, *J. Phys. Chem. C* **2017**, *121*, 9394 – 9401.

[14] B. Sarma, A. L. Jurovitzki, Y. R. Smith, S. K. Mohanty, M. Misra, *ACS Appl. Mater. Interfaces* **2013**, *5*, 1688 – 1697.

[15] G. Kortum, G. Schreyer, *Z. Naturforsch. A* **1957**, *11*, 1018 – 1022.

[16] a) J. Tang, B. Kong, Y. C. Wang, M. Xu, Y. L. Wang, H. Wu, G. F. Zheng, *Nano Lett.* **2013**, *13*, 5350 – 5354; b) S. H. Cho, J. W. Jang, J. W. Kim, J. S. Lee, W. Y. Choi, K. H. Lee, *Langmuir* **2011**, *27*, 10243 – 10250.

[17] H. J. Cao, S. S. Liu, W. W. Tu, J. C. Bao, Z. H. Dai, *Chem. Commun.* **2014**, *50*, 13315 – 13318.

[18] a) I. Robel, B. A. Bunker, P. V. Kamat, *Adv. Mater.* **2005**, *17*, 2458 – 2463; b) F. Wang, W. G. Wang, X. J. Wang, H. Y. Wang, C. H. Tung, L. Z. Wu, *Angew. Chem. Int. Ed.* **2011**, *50*, 3193 – 3197; *Angew. Chem.* **2011**, *123*, 3251 – 3255.

[19] a) J. C. Bian, C. Huang, L. Y. Wang, T. F. Hung, W. A. Daoud, R. Q. Zhang, *ACS Appl. Mater. Interfaces* **2014**, *6*, 4883 – 4890; b) Q. Li, B. D. Guo, J. G. Yu, J. R. Ran, B. H. Zhang, H. J. Yan, J. R. Gong, *J. Am. Chem. Soc.* **2011**, *133*, 10878 – 10884.

[20] a) J. Liu, C. Y. Lu, H. Zhou, J. J. Xu, Z. H. Wang, H. Y. Chen, *Chem. Commun.* **2013**, *49*, 6602 – 6604; b) Z. Yi, H. B. Wang, K. Chen, Q. Gao, H. Tang, R. Q. Yu, X. Chu, *Biosens. Bioelectron.* **2014**, *53*, 310 – 315; c) Y. Li, X. Li, X. T. Ji, X. M. Li, *Biosens. Bioelectron.* **2011**, *26*, 4095 – 4098.

[21] L. Wu, J. S. Wang, J. R. Song, X. G. Qu, *Adv. Funct. Mater.* **2014**, *24*, 2727 – 2733.

Manuscript received: September 10, 2017
Version of record online: ■■ ■■, 0000

COMMUNICATION

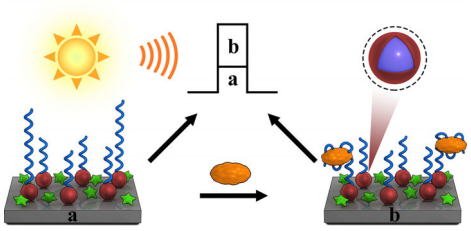

Novel Bi@N,O-codoped carbon core–shell nanohybrids have been synthesized, and shown the typical semiconducting feature. By taking advantage of their excellent photoelectrochemical (PEC) activity and the signal amplification effect of thioflavine-T, a signal on PEC aptasensor for detecting telomerase in HeLa cells is further fabricated, which shows low detection limits, wide linear ranges, high sensitivity and good reproducibility.

Biosensors

S. Liu, S. Zhao, W. Tu, X. Wang, X. Wang, J. Bao, Y. Wang, M. Han, Z. Dai**

■■ – ■■

A Signal on Photoelectrochemical Biosensor Based on Bismuth @N,O-Codoped Carbon Core-Shell Nanohybrids for Ultrasensitive Detection of Telomerase in HeLa Cells